processes

MDPI

Article

How to Effectively Cool Blade Batteries in Extreme High-Temperature Environments?

Li Wang [1], Wenhao Xia [2] and Bin Ding [2,*]

[1] Shanghai Marine Diesel Energy Research Institute, Shanghai 201108, China
[2] College of New Energy, China University of Petroleum (East China), Qingdao 266580, China
* Correspondence: dingbin@upc.edu.cn

Abstract: The market share of blade batteries is rising rapidly due to their high energy density, efficient space utilization, and low cost. Nevertheless, effective cooling solutions for blade batteries are crucial to ensure the safe operation of electric vehicles, especially in extreme high-temperature environments. This paper numerically investigates the effects of a cooling plate and the blade battery parameters on maximum battery temperature, maximum temperature difference, and cooling water pressure drop. Additionally, the energy efficiency of these solutions under various cooling demands is analyzed. The numerical results show that increasing the channel number and changing the flow direction does not significantly improve the cooling performance of the cooling plate. Moreover, the effect of cooling water temperature on the maximum temperature difference in blade batteries is negligible. Furthermore, increasing the cooling water mass flow rate and the rotational speed of the cooling fan is preferred when $T_{max} - T_a > 6$ K, while reducing the cooling water temperature is more energy-efficient when $T_{max} - T_a < 6$ K. These results are expected to offer theoretical guidance and data support for designing cooling systems for blade batteries in extreme high-temperature environments.

Keywords: cooling plate; thermal management; blade battery; energy efficiency analysis

check for updates

Citation: Wang, L.; Xia, W.; Ding, B. How to Effectively Cool Blade Batteries in Extreme High-Temperature Environments? *Processes* **2024**, *12*, 2578. https://doi.org/10.3390/pr12112578

Academic Editor: Jiaqiang E

Received: 4 October 2024
Revised: 31 October 2024
Accepted: 7 November 2024
Published: 17 November 2024

Copyright: © 2024 by the authors. Licensee MDPI, Basel, Switzerland. This article is an open access article distributed under the terms and conditions of the Creative Commons Attribution (CC BY) license (https://creativecommons.org/licenses/by/4.0/).

1. Introduction

New energy vehicles are classified into hybrid electric vehicles and pure electric vehicles, with demand primarily concentrated in China, America, and the European Union [1]. In 2023, global sales of new energy vehicles exceeded 13 million units, representing 16% of the total market share [2]. In China alone, sales surpassed 9.6 million units, capturing a 31.6% market share [3]. Power batteries, the core components of new energy vehicles, supply the electrical energy necessary for driving. Their performance directly impacts key factors such as vehicle range, driving experience, and safety [4,5]. Lithium-ion power batteries are currently categorized by shape into cylindrical, prismatic, and pouch batteries [6,7]. For instance, the 18,650 battery, a cylindrical type, is widely used in Tesla vehicles [8]. To improve battery safety, space utilization, and lifespan, BYD introduced the blade battery (a blade-shaped prismatic battery) in 2020 and incorporated it into the production vehicles [9,10].

It is worth noting that all types of batteries generate a significant amount of heat during operation. If not dissipated promptly, the temperature of the battery can rise rapidly, leading to reduced performance and a shortened lifespan in mild cases, or thermal runaway in severe cases, potentially resulting in fires or explosions [11,12]. The optimal operating temperature for batteries typically ranges between 20 °C and 50 °C, with the maximum internal temperature difference not exceeding 5 °C [13–15]. Scorching weather, particularly temperatures above 35 °C, significantly increases the risk of thermal runaway. In China, such high temperatures can persist for over 45 days each summer, impacting approximately 900 million people [16,17]. Therefore, effective thermal management of lithium-ion power batteries is crucial for ensuring the safe operation of electric vehicles.

Thermal management technologies for power batteries are categorized into air cooling, phase change material (PCM) cooling, liquid cooling, and PCM/liquid hybrid cooling [18,19]. With the rapid increase in power battery capacity and charge/discharge rates, liquid cooling has become the preferred method for meeting heat dissipation requirements [20]. Water cooling plates are often integrated with the battery in a sandwich structure, with thickness reduced to less than 2 mm to conserve space [21]. Enhancing the performance of cooling plates primarily involves increasing the flow rate, lowering water temperature, and optimizing the cooling plate structure [22]. Owing to the significant variability in battery structures, current research mainly focuses on optimizing cooling plate designs to achieve effective thermal management [18,23]. Specifically, cooling plate improvement consists of two aspects, cooling channel structure optimization and cold plate structure optimization.

In terms of cooling channel structure optimization, current research primarily focuses on optimizing cross-sectional shapes (e.g., circular, rectangular, trapezoidal [24]), channel height, and channel width. For instance, Zhang et al. [25] studied the effect of channel shapes on the cooling performance of cooling plates under a constant cross-sectional area. They verified that the trapezoid channel presents the best cooling performance at the same flow rate, while the circular channel results in the maximum pressure drop. Tong et al. [26] demonstrated that increasing the channel height from 0.5 mm to 2 mm can reduce the temperature difference between the prismatic batteries, especially at high discharge rates. However, the effect on the average battery temperature becomes negligible when the thickness exceeds 2 mm. In their study of channel width, Qian et al. [27] found that the pressure drop of the cooling plate decreased by 55% when the channel width increased from 3 mm to 6 mm. Thus, a flow channel with a wide inlet and narrow outlet helps balance cooling performance and pressure drop [28,29]. Notably, increasing the cross-sectional area of the channel while maintaining the same coolant flow rate increases coolant flow, which inevitably increases pumping power. Additionally, the difficulty and cost of fabricating channels with different shapes vary significantly. Therefore, the trade-off between cooling performance, manufacturing cost, and pumping power must be considered when designing the cooling plate.

In terms of cold plate structure optimization, current research primarily focuses on optimizing flow channels (e.g., straight, serpentine, U-bend, pumpkin, spiral, hexagonal), channel number, coolant flow direction, and topology structure [30]. For instance, Monika et al. [31] demonstrated that serpentine and hexagonal channels exhibit a good cooling performance, significantly reducing the maximum temperature and temperature difference of the prismatic battery, despite their high pressure drop. In contrast, the pumpkin-shaped channel effectively reduces pressure drop and pumping power. Similarly, González-Morán et al. [32] and Chen et al. [33] found that serpentine channels outperform straight channels in cooling but result in a higher pressure drop. It is well known that balancing the pressure drop and the cooling performance is challenging, yet few studies focus on comparing the cooling performance of different channels under the same pressure drop conditions. Chen et al. [34] and Ding et al. [35] proved that appropriately increasing the number of channels improves cooling plate performance. Additionally, optimizing the water flow direction in straight channels can further reduce the maximum temperature and temperature difference of the prismatic battery [35]. Similarly, topology optimization can enhance the cooling performance of pre-designed channels. For instance, Chen et al. [36] found that switching from conventional rectangular channels to topology-optimized structures reduced the maximum temperature and temperature difference of the prismatic battery by 0.27% and 19.5%, respectively. However, the high manufacturing cost limits the application of topology-optimized cold plates in power battery thermal management.

It is important to note that the geometric parameters of blade batteries differ significantly from those of traditional prismatic batteries. Specifically, the length of blade batteries can be up to five times that of prismatic batteries, while their width is only half as much. This implies that the thermal entry length effect during the cooling process of blade batteries can be neglected, potentially rendering current cold plate optimization schemes

unsuitable. Unfortunately, most research on cold plate structure optimization focuses on prismatic batteries, with few studies addressing blade batteries [9,24,30]. Moreover, the existing studies mainly set the cooling water temperature as 15–25 °C, with little focus on cooling batteries under extreme high-temperature environments. In this work, some solutions are proposed to effectively cool the blade batteries in extreme high-temperature environments. The effects of the cooling plate and the blade battery parameters on maximum battery temperature, maximum temperature difference, and cooling water pressure drop are numerically investigated. Additionally, the energy efficiency of these solutions under varying cooling demands is analyzed. These results are expected to offer theoretical guidance and data support for designing cooling systems for blade batteries in extreme high-temperature environments.

2. Materials and Methods

2.1. Physical Model

The physical model is shown in Figure 1. The battery system comprises a battery and a cooling plate. Specifically, blade batteries were selected as a commercial model with a capacity of 138 Ah. The nominal voltage and dimensions of the blade batteries are 3.2 V and 960 mm × 90 mm × 12 mm, respectively. To improve cooling performance, an aluminum cooling plate is placed between two adjacent batteries. Specifically, the boundary dimension of the cooling plate is set as 960 mm × 90 mm × 1.5 mm. The cold plate shell thickness is 0.25 mm, and the cross-sectional dimensions of the cooling channel are 89.5 mm × 1.0 mm. Additionally, 0.05 mm thick silicone grease is used to reduce the contact thermal resistance between the cooling plate and the blade battery.

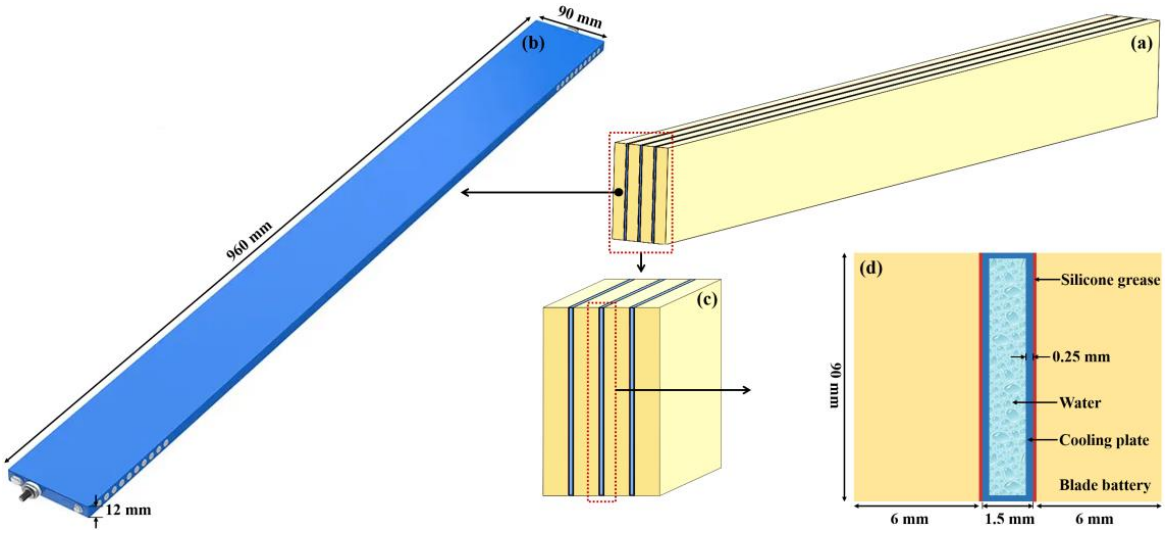

Figure 1. Illustration of physical model.

2.2. Governing Equations and Physical Parameters

To simplify the calculation and simulation process, the following assumptions are made: (1) The internal materials of the blade battery are isotropic, uniformly distributed, and generate heat evenly. (2) Radiation heat transfer is neglected. (3) The cooling water flow in the channel is incompressible. (4) The physical properties of the blade battery's internal materials are temperature-independent. (5) The temperature difference between cooling water and air temperature is ignored. In addition, the maximum value of Reynolds number is 406 in this paper (Re_{max} = 406 < 2300), that is, the cooling water follows a laminar flow in the cooling plate. In summary, the continuity, mass, and energy conservation equations for the cooling water are expressed as follows [12,22]:

$$\frac{\partial}{\partial \tau}\left(\rho_w \vec{v}\vec{v}\right) = -\nabla p \quad (1)$$

$$\frac{\partial \rho_w}{\partial \tau} + \nabla\left(\rho_w \vec{v}\right) = 0 \quad (2)$$

$$\frac{\partial}{\partial \tau}\left(\rho_w c_{pw} T_w\right) + \nabla\left(\rho_w c_{pw} T_w \vec{v}\right) = -\nabla(\lambda_w \nabla T_w) \quad (3)$$

Moreover, the energy conservation equations for the cooling plate and battery are expressed as follows [12,22]:

$$c_{pc}\rho_c \frac{\partial T_c}{\partial \tau} = -\lambda_c \nabla(\nabla T_c) \quad (4)$$

$$c_{pb}\rho_b \frac{\partial T_b}{\partial \tau} = -\lambda_b \nabla(\nabla T_b) + \frac{Q}{V} \quad (5)$$

where Q represents the heat generation power of the blade battery; V is the volume of the blade battery; T is the temperature (K); c_p is the specific heat capacity; λ is the thermal conductivity; ρ is the density; τ is the time; p is the pressure; $\vec{v}$ is the velocity vector of cooling water; and the subscript w, c, and b represent cooling water, cooling plate, and battery, respectively. In addition, the physical parameters of the cooling water, cooling plate, blade battery, and silicone grease are shown in Table 1.

Table 1. Physical parameters of the model.

Parameters	c_p (J·kg^{-1}·K^{-1})	ρ (kg·m^{-3})	λ (W·m^{-1}·K^{-1})
Cooling water	4218	998.2	0.6
Cooling plate	871	2719	202.4
Blade battery	1108	2450	3.9
Silicone grease	-	-	2.5 [37]

2.3. Boundary Conditions

In this model, the cooling water inlet is set as a velocity inlet, and the outlet is defined as a standard atmospheric pressure outlet. A coupled boundary is defined at the interface between the cooling plate and the battery, and a fluid–structure interaction boundary is applied at the interface between the cooling plate and the water. The battery's outer wall is defined as an adiabatic no-slip boundary. Moreover, the battery is set as a uniformly distributed internal heat source. To ensure computational accuracy, the SIMPLE algorithm is utilized to couple the iteration of the pressure and velocity fields, while the discretized equations employ a second-order upwind scheme. Convergence is considered achieved when the residuals drop to 10^{-4}.

2.4. Model Validation

In this study, ANSYS FLUENT 2020R2 was employed to simulate the cooling process of blade batteries. The ICEM method was utilized to mesh the blade battery model. Initially, the blade battery model was constructed using SpaceClaim 2020 R2, comprising multiple blade batteries clamped between cooling plates. Each cooling plate cools half of the battery cells on either side. To simplify the computations and reduce simulation time, the model of multiple batteries and liquid cooling channels was simplified. The simplified model consists of one cooling plate and two half-cell units. Adiabatic boundary conditions were applied to the model surface to represent a symmetrical battery model, as shown in Figure 1d. The symmetrical blade model was subsequently imported into ICEM CFD 2020 R2. The time step was set as 0.2 s with a total of 3600 steps. Furthermore, the maximum temperature within the blade battery (T_{max}) and the pressure drop (Δp) at the end of the discharging process were chosen to verify grid independence. Figure 2a shows the evolutions of T_{max} and Δp for different grid numbers. It can be observed that T_{max} and Δp increase progressively as the grid number rises from 0.72 to 2.65 million. Beyond this point, further increases in the grid number have no significant effect on T_{max} and Δp. Therefore, to balance convergence speed and computational accuracy, a grid number of 2.65 million was selected for this work.

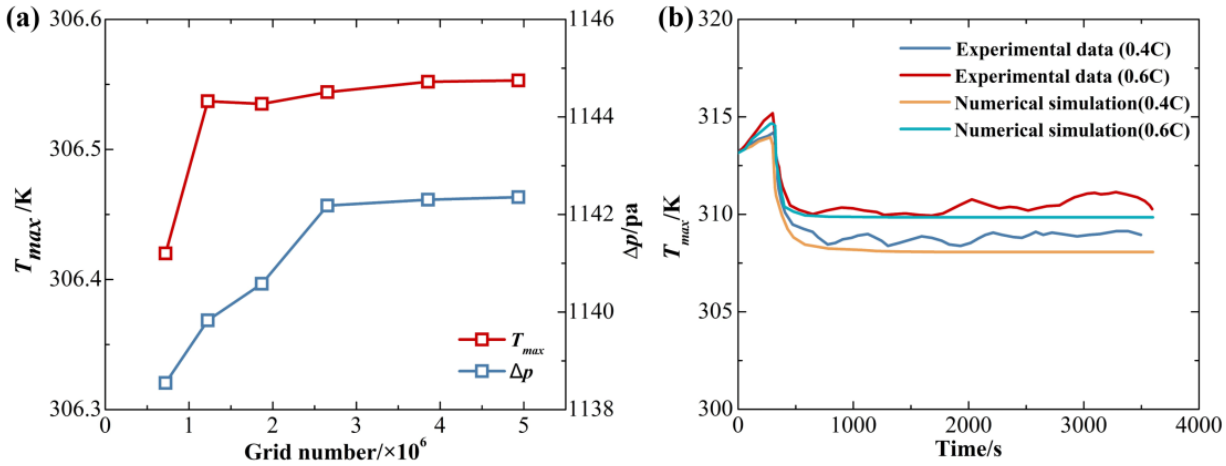

Figure 2. (**a**) Evolutions of T_{max} and Δp under various grid numbers, (**b**) Comparisons between present simulation and experimental result of Xu et al. [38].

Before performing the calculations, an experimental case of a single-phase microchannel heat sink, provided by Xu et al. [38], was selected to validate the model's performance in terms of flow and heat transfer. The comparison between simulation and experimental results is presented in Figure 2b, demonstrating the evolution of T_{max} during the discharging process. The simulation results show good agreement with the experimental data, with a maximum error of 0.82%.

3. Results and Discussion

3.1. Effect of Channel Number on Cooling Performance

The cooling performance of the cooling plate generally improves with an increase in the number of channels. To further investigate the influence of channel number on the cooling performance of blade batteries, the discharge rate, cooling water temperature, and mass flow rate were set at 4C (q = 160 kW·m^{-3}), T_w = 298.15 K, and M = 8 g·s^{-1}, respectively. Figure 3a illustrates the temperature distribution of the blade battery cooled by a single-channel cooling plate (N = 1). It is evident that the battery temperature increases along the flow direction, with the temperature near the outlet position rising gradually during the discharge process. In contrast, the increase in battery temperature near the inlet position can be considered negligible. Eventually, the temperature distribution within the blade battery stabilizes at τ > 240 s. Additionally, the maximum temperature (T_{max}) and the maximum temperature difference (ΔT_{max}) are presented in Figure 3b to facilitate a more comprehensive analysis of the temperature distribution within the blade battery. The results indicate that T_{max} and ΔT_{max} increase to 304.26 K and 5.86 K, respectively, during the discharge process. Notably, the ΔT_{max} exceeds the acceptable limits, posing a risk to the safe operation of the blade batteries.

To enhance the cooling performance of the cooling plate, we increased the channel number. Figure 4 illustrates the effects of channel number (N) on T_{max}, ΔT_{max}, and the pressure drop of the cooling water between the inlet and outlet (Δp) at τ = 420 s. The results show that both T_{max} and ΔT_{max} increase by 0.04 K as the channel number rises from N = 1 to N = 9. Furthermore, Δp increases by approximately 5.3% with the increase in channel number. In channels with narrow widths, augmenting the channel number has a limited impact on the heat transfer area, but it significantly reduces the cross-sectional flow area for the cooling water, resulting in an increased flow velocity and pressure drop. The convective heat transfer coefficient of laminar flow is independent of the cooling water's flow velocity. By contrast, it increases with a higher length-to-width ratio of the rectangular flow section but decreases with an increase in hydraulic diameter. Specifically, as the channel number increased from 1 to 9, the hydraulic diameter decreased from 1.98 mm to 1.82 mm, while the length-to-width ratio decreased from 90 to 10. Additionally, the total heat transfer area

rose by approximately 6.6% with the increase in channel number from 1 to 9. Nevertheless, the cooling performance improvement was negligible as the channel number increased from 1 to 9. This suggests that reducing the cooling plate thickness may be a more effective approach to enhancing cooling performance.

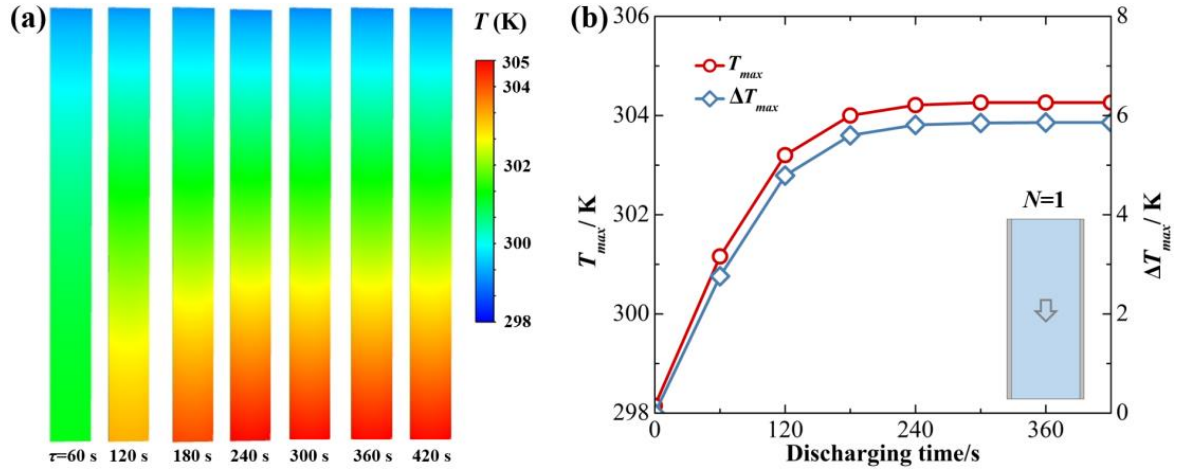

Figure 3. (**a**) Temperature distribution of blade battery (N = 1), (**b**) Evolution of battery maximum temperature and maximum temperature difference.

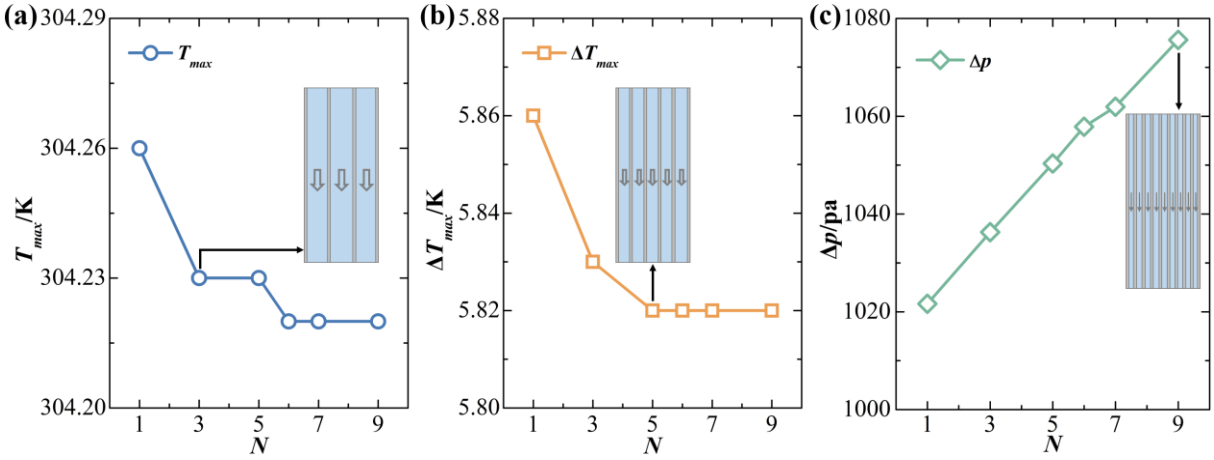

Figure 4. Effect of channel number on maximum battery temperature (**a**), maximum temperature difference (**b**), and cooling water pressure drop (**c**) in a steady state (τ = 420 s).

3.2. Effect of Flow Direction on Cooling Performance

Previous research proved that changing the flow direction from parallel flow to counter flow is another effective way to improve the cooling performance of the cooling plate. Therefore, we chose three cases (N = 5, 6, and 7, as shown in Figure 5a) to verify their suitability on cooling blade batteries. Moreover, the discharging rate, cooling water temperaturte, and mass flow rate are still set as 4C (q = 160 kW·m^{-3}), T_w = 298.15 K, M = 8 g·s^{-1}, respectively. Figure 5b shows the temperature distribution of the blade battery under various flow directions. One can see that the T_{max} is present at the central position of the blade battery under a counter flow direction. Moreover, the temperature distribution becomes uneven in the width direction. What is even worse, the counter flow increases the T_{max} and ΔT_{max}, and their values increase gradually with an increase in the channel number. Specifically, Figure 5c,d proves that the T_{max} and ΔT_{max} increases about 4.21 K and 2.02 K, respectively, after changing the flow direction and increasing the channel number. In the cases of counter flow, both ends of the blade battery are mainly cooled by the water in the inlet channels, making the cooling water present a peak value at the central position of the blade battery. In

conclusion, the counter flow not only fails to improve the cooling effect of the cold plate on the blade battery but also increases the manufacturing cost of the cooling water circulation system. Therefore, the cooling plate of N = 1 is the preferred plan followed to balance the cooling performance of the blade batteries and the manufacturing cost.

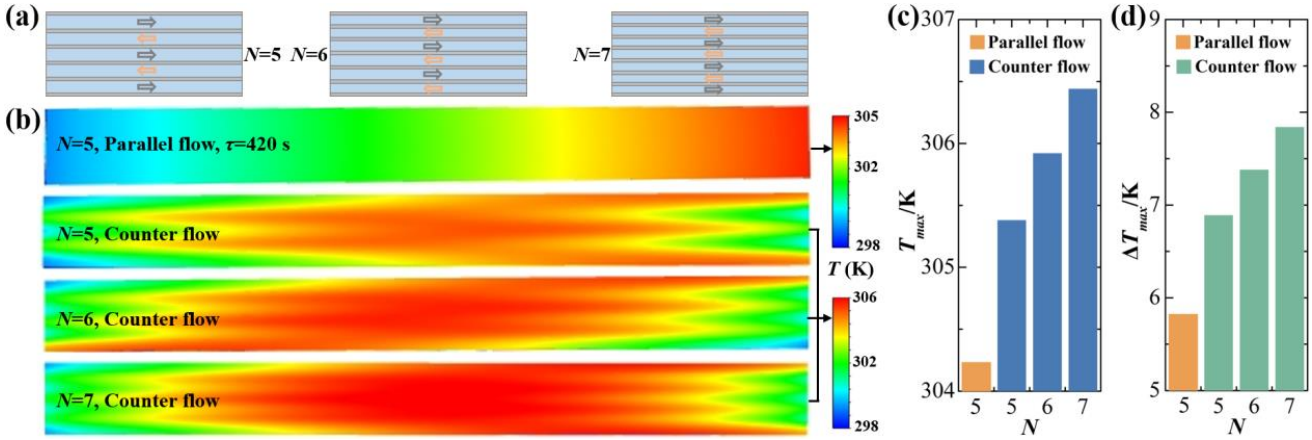

Figure 5. (**a**) Illustration of cooling water flow direction in cooling plate, (**b**) Temperature distribution of blade battery, (**c**) Evolution of battery maximum temperature under various flow directions and channel numbers, (**d**) Maximum temperature difference under various flow directions and channel numbers.

Previous research [35,39,40] has demonstrated that altering the flow direction from parallel to counter flow is an effective method for enhancing the cooling performance of cooling plates. Accordingly, we selected three cases (N = 5, 6, and 7, as illustrated in Figure 5a) to assess their suitability for cooling blade batteries. The discharge rate, cooling water temperature, and mass flow rate were maintained at 4C (q = 160 kW·m^{-3}), T_w = 298.15 K, M = 8 g·s^{-1}, respectively. Figure 5b presents the temperature distribution of the blade battery under various flow directions. Notably, T_{max} is positioned centrally within the blade battery under counter flow conditions. Moreover, the temperature distribution exhibits unevenness across the width. Additionally, counter flow increases T_{max} and ΔT_{max}, with both values rising progressively with the channel number. Specifically, Figure 5c,d indicate that T_{max} and ΔT_{max} increase by approximately 4.21 K and 2.02 K, respectively, following the change in flow direction and channel number increment. In counter flow scenarios, the ends of the blade battery are primarily cooled by the water in the inlet channels, resulting in a peak temperature at the center of the battery. In conclusion, counter flow not only fails to enhance the cooling performance of the cold plate on the blade battery but also raises the manufacturing cost of the cooling water circulation system. Therefore, a cooling plate configuration of N = 1 is the preferred solution to balance the cooling performance and the manufacturing cost for blade batteries.

3.3. Effect of Discharging Rate on Cooling Performance

The discharging rates of blade batteries vary significantly across different application scenarios. To investigate the cooling performance at various discharging rates (2C~5C, q = 80~200 kW·m^{-3}), the cooling water temperature and mass flow rate were maintained at T_w = 298.15 K and M = 14 g·s^{-1}, respectively. The effects of the discharging rate on T_{max}, ΔT_{max}, and the cooling water temperature difference between the inlet and outlet (ΔT_w) are presented in Figure 6. It is evident that T_{max} increases linearly from 300.15 K to 303.15 K as the discharging rate rises from 2C to 5C. Similarly, ΔT_{max} increases linearly from 1.89 K to 4.73 K. Notably, ΔT_w also rises from 1.42 K to 3.54 K, attributed to the increase in the heat generation rate with higher discharging rates. The influence of temperature variation on physical parameters can be neglected as the discharging rate increases from 2C to 5C, indicating that the convective heat transfer coefficient remains unaffected by

discharge rate changes. Applying Newton's law of cooling and the principle of energy conservation yields the equation $q = hA\Delta T = c_p M \Delta T_w$, demonstrating that T_{max}, ΔT_{max} and ΔT_w are proportional to the discharging rate. Therefore, to maintain the safe operation of the blade battery at higher discharge rates, enhancing the cooling performance is essential, which can be achieved by either increasing the coolant flow rate or decreasing the cooling water temperature.

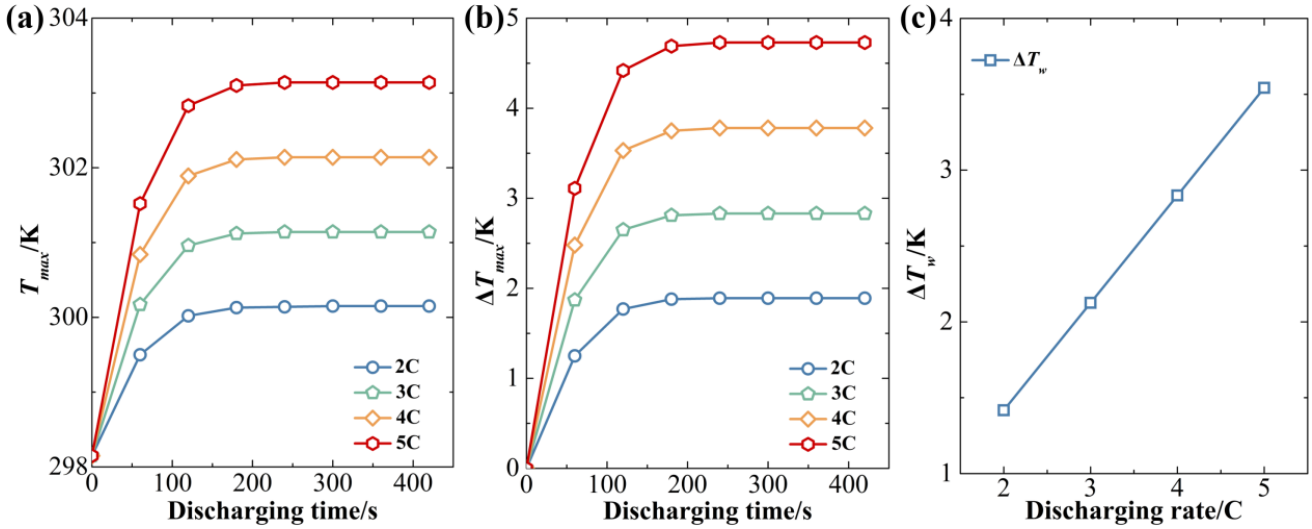

Figure 6. Effect of discharging rate on maximum battery temperature (**a**), maximum temperature difference (**b**), and cooling water temperature difference between inlet and outlet (**c**) in a steady state (N = 1, τ = 420 s).

3.4. Effect of Cooling Water Mass Flow Rate on Cooling Performance

To investigate the cooling performance at various cooling water mass flow rates, the cooling water temperature and discharging rate were maintained at T_w = 298.15 K and 5C, respectively. The effects of mass flow rate on ΔT_w, T_{max}, and ΔT_{max} are presented in Figure 7a. It is observed that T_{max}, ΔT_{max} and ΔT_w all decrease about 2 K when the M increases from 8 g·s^{-1} to 12 g·s^{-1}. By contrast, they only decrease by about 1 K when the M further increases to 16 g·s^{-1}. This indicates that the improvement in cooling performance diminishes as the mass flow rate of the cooling water increases. Generally, increasing the cooling water mass flow rate enhances the convective heat transfer coefficient (h) and reduces the ΔT_w. However, for the cases considered in this study, h remains constant due to the laminar flow condition and negligible thermal entry length effect. Consequently, T_{max}, ΔT_{max}, and ΔT_w are all proportional to M^{-1}, as depicted in Figure 7b. It is important to note that an increase in the mass flow rate inevitably leads to a rise in the pressure drop. Figure 7c proves that the Δp linearly increases with mass flow rate, specifically, by 128 Pa for every 1 g·s^{-1} increase. Moreover, the pump power is proportional to both Δp and M. That means, the pump power increases by about 1.25 and 3.01 times when the M increases from 8 g·s^{-1} to 12 g·s^{-1} and 16 g·s^{-1}, respectively. In conclusion, as the cooling water flow rate increases, the improvements in cooling performance diminish rapidly, while the pump power consumption escalates significantly. Therefore, varying the cooling water mass flow rate alone is not an adequate solution for cooling blade batteries.

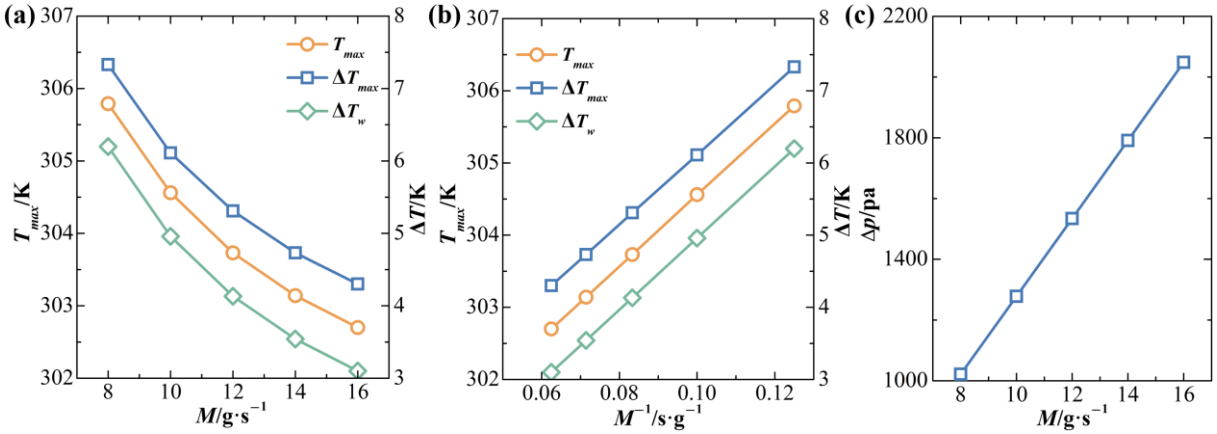

Figure 7. Effect of cooling water mass flow rate on maximum battery temperature, maximum temperature difference, cooling water temperature difference between inlet and outlet (**a**,**b**), and cooling water pressure drop (**c**) in a steady state (N = 1, τ = 420 s).

3.5. Effect of Cooling Water Temperature on Cooling Performance

The temperature of the cooling water is governed by the ambient temperature, which plays a crucial role in enhancing the cooling performance of the cooling plate, particularly under extreme high-temperature conditions. To comprehensively investigate the effect of the cooling water temperature (T_w = 293.15~308.15 K) on cooling performance, the mass flow rate of the cooling water and the discharging rate were maintained at M = 14 g·s^{-1} and 5C, respectively. Figure 8 illustrates the distribution of T_{max}, ΔT_{max}, and ΔT_w under various cooling water temperatures. It is evident that T_{max} increases linearly with rising cooling water temperature, with a 1 K increase in T_{max} for each 1 K rise in cooling water temperature. In contrast, both ΔT_{max} and ΔT_w remain unaffected by changes in cooling water temperature. This indicates that variations in physical parameters can be ignored when cooling water temperature increases from 293.15 K to 308.15 K. Thus, the convective heat transfer coefficient can be considered constant. In conclusion, T_{max} can be reduced by either increasing the cooling water mass flow rate or decreasing the discharging rate and cooling water temperature. However, ΔT_{max} is solely influenced by the discharging rate and cooling water mass flow rate.

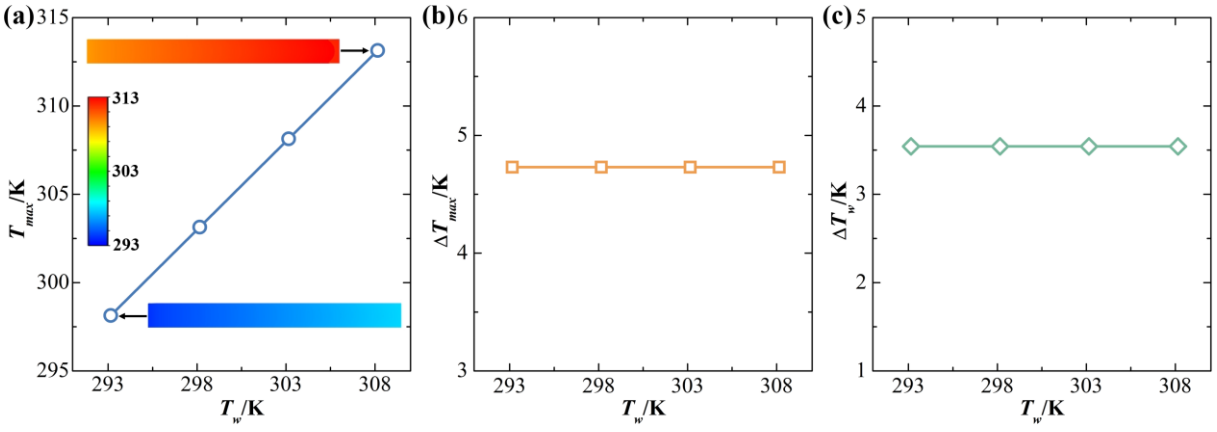

Figure 8. Effect of cooling water temperature on maximum battery temperature (**a**), maximum temperature difference (**b**), and cooling water temperature difference between inlet and outlet (**c**) in a steady state (N = 1, τ = 420 s).

It is important to note that the heat generated by blade batteries will eventually dissipate into the environment, regardless of the cooling method used. This means that the cooling water temperature will always be at least 3 K higher than the ambient temperature

(T_a) [41], which poses significant challenges for thermal management of blade batteries under extreme conditions (5C, $T_w \geq 308.15$ K), particularly for batteries with a lower maximum temperature threshold (313.15 K $\leq T_{max} \leq$ 318.15 K). Under such extreme conditions, merely increasing the cooling water mass flow rate and the rotational speed of the cooling fan may not be sufficient to meet the cooling requirements of blade batteries. To address the challenges posed by global warming and facilitate the adoption of electric vehicles in tropical desert regions, it is imperative to explore new methods for enhancing cooling performance. Potential solutions include lowering the cooling water temperature using air conditioning or thermoelectric cooling.

3.6. Cooling Performance Prediction and Energy Efficiency Analysis

Before analyzing the energy efficiency of various cooling methods, it is crucial to make an accurate prediction of the cooling plate's performance. Based on the comprehensive analysis in Sections 3.1–3.5, correlations between the battery's maximum temperature (T_{max}), maximum temperature difference (ΔT_{max}), and cooling water pressure drop (Δp) were established by fitting simulated data as follows:

$$T_{\max} = 1.084 T_w^{0.984} M^{-0.0134} q^{0.0117} \tag{6}$$

$$\Delta T_{\max} = 0.184 M^{-0.778} q \tag{7}$$

$$\Delta p = 128.35 M - 5.572 \tag{8}$$

As depicted in Figure 9, the correlations (Equations (6)–(8)) align well with the simulated data, with R-squared values (R^2) of 0.997, 1.0 and 1.0, respectively.

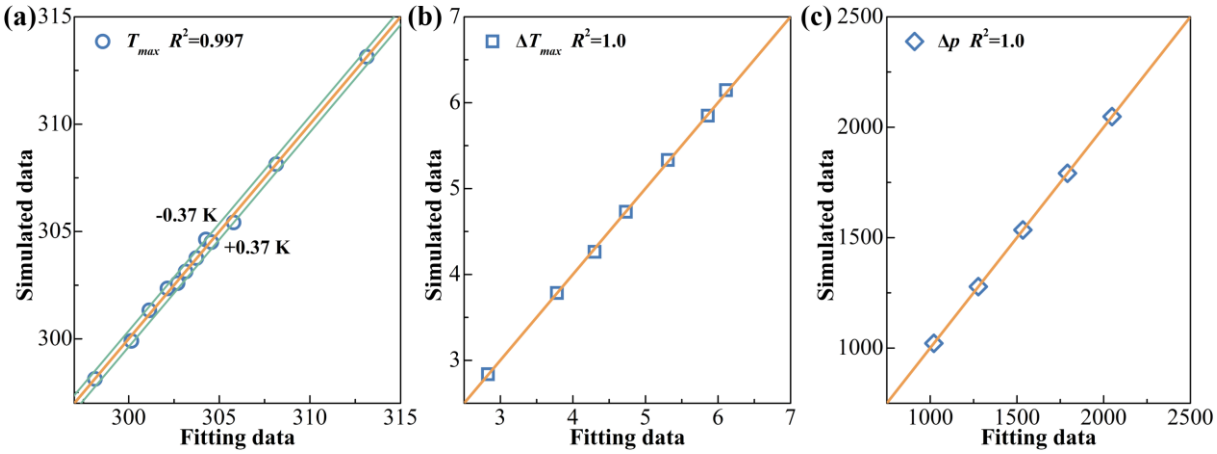

Figure 9. Divergence between the correlations and the simulated data.

Under typical extreme conditions (T_a = 308.18 K, 5C, Q = 207.36 W) and various cooling demands (313.15 K $\leq T_{max} \leq$ 318.15 K, $\Delta T_{max} \leq$ 5 K, $\Delta T_{wb} = T_{max} - T_w \geq$ 1 K), the relationship between T_w and M is deduced and shown in Figure 10. The cooling method that increases the cooling water mass flow rate and the rotational speed of the cooling fan is defined as Mode 1, whereas lowering the cooling water temperature using air conditioning or thermoelectric cooling is defined as Mode 2. The total power of the cooling system (P) includes both pumping power and cooling power, expressed as:

$$P = \frac{M}{\rho_w \eta_p} \Delta p + \frac{qV}{\eta} \tag{9}$$

$$\eta = \begin{cases} 0.72(T_w - T_a) & \text{Mode 1} \\ 3.5 & \text{Mode 2} \end{cases} \tag{10}$$

where η is the energy efficiency ratio and η_p = 0.5 represents the pump efficiency. Previous studies [42–45] have shown that the energy efficiency ratio of the cooling fan can be simplified to $\eta = 0.72(T_w - T_a)$. Moreover, the energy efficiency ratio of vehicle power conditioners ranges from 2 to 5 [46,47]. By comparison, the energy efficiency ratio of thermoelectric cooling rarely exceeds 1 in extreme high-temperature environments [48]. Therefore, η = 3.5 is selected to represent Mode 2.

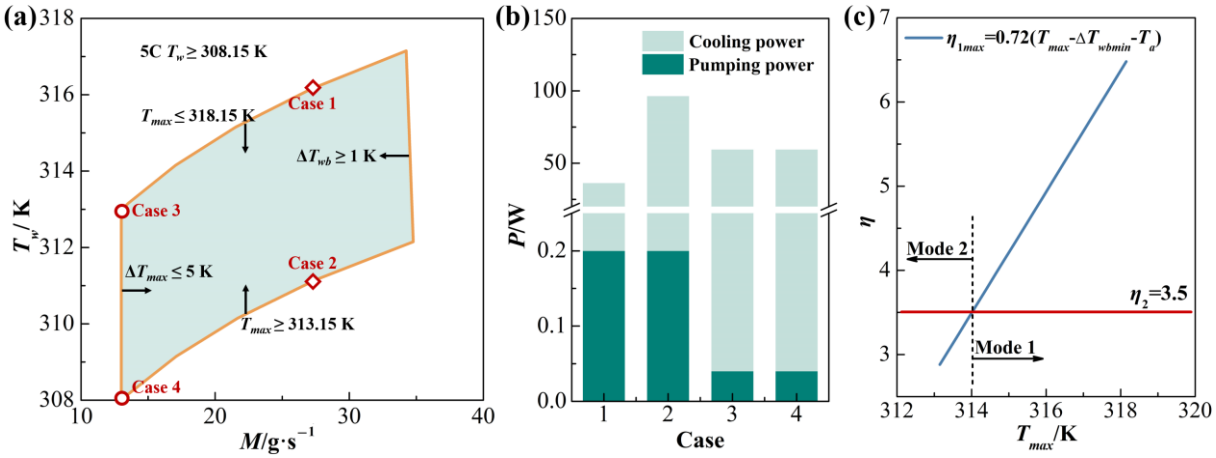

Figure 10. (**a**) Cooling conditions needed for achieving various demands (313.15 K $\leq T_{max} \leq$ 318.15 K, $\Delta T_{max} \leq$ 5 K, $\Delta T_{wb} = T_{max} - T_w \geq$ 1 K), (**b**) Pumping power and cooling power of the four cases, (**c**) Distribution of energy efficiency ratio under various cooling modes.

Four cases were chosen to analyze the energy efficiency of various cooling modes, and the detailed parameters are shown in Table 2. It can be seen that P = 96.2 W is required under Mode 1 to maintain T_{max} = 313.15 K. In contrast, P decreases to 36.2 W when T_{max} rises to 318.15 K. It is noteworthy that P = 59.3 W in Mode 2 is independent of T_{max}, meaning that Mode 2 is recommended for blade batteries with a lower maximum temperature (e.g., T_{max} = 313.15 K), whereas Mode 1 is more suitable for higher maximum temperatures (e.g., T_{max} = 318.15 K). Additionally, the pumping power and cooling power for these cases are calculated and shown in Figure 10b, indicating that cooling power dominates the total power of the cooling system, and the proportion of pumping power is negligible. Therefore, the maximum energy efficiency ratio for Mode 1 can be approximately expressed as follows:

$$\eta_{1\max} = 0.72(T_{\max} - \Delta T_{wb\min} - T_a) \quad (11)$$

where ΔT_{wbmin} = 1 is the minimum temperature difference between the blade batteries and the cooling water. Figure 10c illustrates the energy efficiency ratio distribution for various cooling modes. It demonstrates that increasing the cooling water mass flow rate and the rotational speed of the cooling fan is preferred for cooling blade batteries when $T_{max} - T_a > 6$ K, whereas reducing the cooling water temperature is a more energy-efficient solution when $T_{max} - T_a < 6$ K. These results are expected to provide theoretical guidance and data support for designing cooling systems for blade batteries in extreme high-temperature environments.

Table 2. Detailed parameters of the four cases.

Cooling Mode		T_{max}/K	ΔT_{max}/K	T_w/K	M/g·s^{-1}	Δp/Pa	η	P/W
Mode 1	Case 1	318.15	≤5	316.15	27.4	3511	5.76	36.2
	Case 2	313.15	≤5	311.15	27.4	3511	2.16	96.2
Mode 2	Case 3	318.15	≤5	313.15	13	1663	3.5	59.3
	Case 4	313.15	≤5	308.15	13	1663	3.5	59.3

4. Conclusions

In this paper some solutions are proposed to effectively cool blade batteries in extreme high-temperature environments. The effects of the cooling plate and the blade battery parameters on maximum battery temperature, maximum temperature difference, and cooling water pressure drop are thoroughly examined. Additionally, the energy efficiency of these solutions under varying cooling demands is analyzed. The main conclusions drawn from the results and discussions are as follows:

(1) Increasing the number of channels and altering the flow direction does not significantly enhance the cooling performance of the cooling plate.
(2) The effect of the cooling water temperature on the maximum temperature difference of blade batteries is negligible.
(3) Correlations between cooling plate parameters, blade battery parameters, and cooling performance were established to address gaps in theoretical predictions.
(4) Increasing the mass flow rate of the cooling water and the rotational speed of the cooling fan is recommended for cooling blade batteries, when the temperature difference between the maximum temperature inside the battery and the ambient temperature exceeds 6 K ($T_{max} - T_a > 6$ K). Conversely, when the temperature difference is less than 6 K, reducing the cooling water temperature is a more energy-efficient approach.
(5) To better cool blade batteries, future research should focus on reducing the thickness of the cooling plate and developing new coolants.

Author Contributions: Conceptualization, L.W.; methodology, W.X.; software, W.X.; validation, L.W.; investigation, B.D.; data curation, L.W.; writing—original draft preparation, L.W. and B.D.; writing—review and editing, B.D.; project administration, B.D.; funding acquisition, B.D. All authors have read and agreed to the published version of the manuscript.

Funding: This work was supported by the National Natural Science Foundation of China (No. 52276091).

Data Availability Statement: The original contributions presented in the study are included in the article, further inquiries can be directed to the corresponding author.

Conflicts of Interest: The authors declare no conflicts of interest.

References

1. Yu, Z.; Zhang, J.; Pan, W. A review of battery thermal management systems about heat pipe and phase change materials. *J. Energy Storage* **2023**, *62*, 106827. [CrossRef]
2. Jiang, F.; Yuan, X.; Hu, L.; Xie, G.; Zhang, Z.; Li, X.; Hu, J.; Wang, C.; Wang, H. A comprehensive review of energy storage technology development and application for pure electric vehicles. *J. Energy Storage* **2024**, *86*, 111159. [CrossRef]
3. Li, X.; Wang, Z.Y.; Jiang, S.M.; Li, C.Y.; Guo, H.X. Financial subsidy, government audit and new transportation technology: Evidence from the new energy vehicle pilot city program in China. *Res. Transp. Econ.* **2024**, *106*, 101447. [CrossRef]
4. Mu, M.F.; Sui, P.X.; Kou, G.Y.; Ding, B.; Han, Z.L.; Sun, K.; Zhang, Q.; Hu, X.D. Numerical study of positive temperature coefficient heating on the lithium-ion battery at low temperature. *AIP Adv.* **2024**, *14*, 035303. [CrossRef]
5. Acar, E.; Jain, N.; Ramu, P.; Hwang, C.; Lee, I. A survey on design optimization of battery electric vehicle components, systems, and management. *Struct. Multidiscip. Optim.* **2024**, *67*, 27. [CrossRef]
6. Altuntepe, A.; Erkan, S.; Olgar, M.A.; Celik, S.; Zan, R. Investigating surface area and hydrogen pressure effects on LiH and NaH. *J. Solid State Chem.* **2024**, *330*, 124483. [CrossRef]
7. Wu, W.X.; Wang, S.F.; Wu, W.; Chen, K.; Hong, S.H.; Lai, Y.X. A critical review of battery thermal performance and liquid based battery thermal management. *Energy Convers. Manag.* **2019**, *182*, 262–281. [CrossRef]
8. Zhu, S.X.; Yang, L.; Wen, J.W.; Feng, X.L.; Zhou, P.J.; Xie, F.G.; Zhou, J.; Wang, Y.N. In operando measuring circumferential internal strain of 18650 Li-ion batteries by thin film strain gauge sensors. *J. Power Sources* **2021**, *516*, 230669. [CrossRef]
9. Chen, F.; Zhu, W.; Kong, X.; Huang, Y.; Wang, Y.; Zheng, Y.; Ren, D. Study on the Homogeneity of Large-Size Blade Lithium-Ion Batteries Based on Thermoelectric Coupling Model Simulation. *Energies* **2022**, *15*, 9556. [CrossRef]
10. Altuntepe, A.; Erkan, S.; Olgar, M.A.; Celik, S.; Zan, R. Hydrogen storage capacity of two-dimensional MoS_2. *Int. J. Hydrogen Energy* **2024**, *56*, 690–698. [CrossRef]
11. Hussain, M.T.; Bin Sulaiman, N.; Hussain, M.S.; Jabir, M. Optimal Management strategies to solve issues of grid having Electric Vehicles (EV): A review. *J. Energy Storage* **2021**, *33*, 102114. [CrossRef]

12. Shen, X.Y.; Zhang, X.Z.; Pan, H.R.; Chen, M. Thermal management of Li-ion battery based on honeycomb-structured fins-modified phase change material. *Int. J. Heat Mass Transf.* **2024**, *232*, 125962. [CrossRef]
13. Wagh, V.A.; Saha, S.K. Optimising extended fin design and heat transfer coefficient for improved heat transfer and PCM recover time in thermal management of batteries. *Appl. Therm. Eng.* **2024**, *255*, 123964. [CrossRef]
14. Wang, Z.B.; Wang, Y.L.; Qin, J.Y.; Chen, Z.Z.; Ding, B.; Chen, Y. Core release dynamics of double-emulsion droplets induced by temperature gradient. *Phys. Fluids* **2024**, *36*, 052004. [CrossRef]
15. Wang, Z.B.; Li, Z.L.; Jia, L.S.; Ding, B.; Chen, Y. Numerical Investigation on Heat Transfer Characteristics of Microencapsulated Phase Change Material Slurry in a Rectangular Minichannel. *J. Therm. Sci.* **2024**, *33*, 564–577. [CrossRef]
16. Shi, X.H.; Lu, C.G.; Xu, X.D. Variability and Trends of High Temperature, High Humidity, and Sultry Weather in the Warm Season in China during the Period 1961-2004. *J. Appl. Meteorol. Clim.* **2011**, *50*, 127–143. [CrossRef]
17. Ding, T.; Ke, Z.J. Characteristics and changes of regional wet and dry heat wave events in China during 1960–2013. *Theor. Appl. Climatol.* **2015**, *122*, 651–665. [CrossRef]
18. Zhao, G.; Wang, X.; Negnevitsky, M.; Li, C. An up-to-date review on the design improvement and optimization of the liquid-cooling battery thermal management system for electric vehicles. *Appl. Therm. Eng.* **2023**, *219*, 119626. [CrossRef]
19. Gharehghani, A.; Rabiei, M.; Mehranfar, S.; Saeedipour, S.; Andwari, A.M.; García, A.; Reche, C.M. Progress in battery thermal management systems technologies for electric vehicles. *Renew. Sustain. Energy Rev.* **2024**, *202*, 114654. [CrossRef]
20. Zhang, F.R.; Tao, Y.B.; He, Y.X.; Qiu, S.S. Optimization and thermal characterization of a new liquid-cooled plate with branching channels of fractal geometry. *Appl. Therm. Eng.* **2024**, *254*, 123881. [CrossRef]
21. Sui, Z.G.; Lin, H.S.; Sun, Q.; Dong, K.J.; Wu, W. Multi-objective optimization of efficient liquid cooling-based battery thermal management system using hybrid manifold channels. *Appl. Energy* **2024**, *371*, 123766. [CrossRef]
22. Zhan, S.; Chen, Y.; Yin, Y.L.; Li, Z.H.; Yu, C. Examining the influence of number of inlets and outlets on the topology optimization design of battery liquid cooling plate. *Appl. Therm. Eng.* **2024**, *252*, 123691. [CrossRef]
23. Chen, H.P.; Zhang, T.S.; Han, Z.W.; Huang, H.Z.; Chen, H.B.; Gao, Q. Battery thermal management enhancement based on bionics. *Int. Commun. Heat Mass* **2024**, *157*, 107756. [CrossRef]
24. Deng, Y.; Feng, C.; Jiaqiang, E.; Zhu, H.; Chen, J.; Wen, M.; Yin, H. Effects of different coolants and cooling strategies on the cooling performance of the power lithium ion battery system: A review. *Appl. Therm. Eng.* **2018**, *142*, 10–29. [CrossRef]
25. Zhang, Y.; Wang, S.; Ding, P. Effects of channel shape on the cooling performance of hybrid micro-channel and slot-jet module. *Int. J. Heat Mass Transf.* **2017**, *113*, 295–309. [CrossRef]
26. Tong, W.; Somasundaram, K.; Birgersson, E.; Mujumdar, A.S.; Yap, C. Numerical investigation of water cooling for a lithium-ion bipolar battery pack. *Int. J. Therm. Sci.* **2015**, *94*, 259–269. [CrossRef]
27. Qian, Z.; Li, Y.M.; Rao, Z.H. Thermal performance of lithium-ion battery thermal management system by using mini-channel cooling. *Energy Convers. Manag.* **2016**, *126*, 622–631. [CrossRef]
28. Karimi, G.; Dehghan, A.R. Thermal analysis of high-power lithium-ion battery packs using flow network approach. *Int. J. Energy Res.* **2014**, *38*, 1793–1811. [CrossRef]
29. Choi, J.; Kim, Y.-H.; Lee, Y.; Lee, K.-J.; Kim, Y. Numerical analysis on the performance of cooling plates in a PEFC. *J. Mech. Sci. Technol.* **2008**, *22*, 1417–1425. [CrossRef]
30. Jiang, Z.Y.; Li, H.B.; Qu, Z.G.; Zhang, J.F. Recent progress in lithium-ion battery thermal management for a wide range of temperature and abuse conditions. *Int. J. Hydrogen Energy* **2022**, *47*, 9428–9459. [CrossRef]
31. Monika, K.; Datta, S.P. Comparative assessment among several channel designs with constant volume for cooling of pouch-type battery module. *Energy Convers. Manag.* **2022**, *251*, 114936. [CrossRef]
32. González-Morán, L.; Suárez, C.; Iranzo, A.; Han, L.; Rosa, F. A numerical study on heat transfer for serpentine-type cooling channels in a PEM fuel cell stack. *Energy* **2024**, *307*, 132634. [CrossRef]
33. Chen, F.C.; Gao, Z.; Loutfy, R.O.; Hecht, M. Analysis of Optimal Heat Transfer in a PEM Fuel Cell Cooling Plate. *Fuel Cells* **2004**, *3*, 181–188. [CrossRef]
34. Chen, K.; Chen, Y.; Song, M.; Wang, S. Multi-parameter structure design of parallel mini-channel cold plate for battery thermal management. *Int. J. Energy Res.* **2020**, *44*, 4321–4334. [CrossRef]
35. Ding, B.; Qi, Z.H.; Mao, C.S.; Gong, L.; Liu, X.L. Numerical investigation on cooling performance of PCM/cooling plate hybrid system for power battery with variable discharging conditions. *J. Therm. Anal. Calorim.* **2020**, *141*, 625–633. [CrossRef]
36. Chen, F.; Wang, J.; Yang, X.L. Topology optimization design and numerical analysis on cold plates for lithium-ion battery thermal management. *Int. J. Heat Mass Transf.* **2022**, *183*, 122087. [CrossRef]
37. Gou, Y.; Liu, Z.; Zhang, G.; Li, Y. Effects of multi-walled carbon nanotubes addition on thermal properties of thermal grease. *Int. J. Heat Mass Transf.* **2014**, *74*, 358–367.
38. Xu, J.; Zhou, T.; Xu, X. Experimental investigation on a novel liquid cooling device for a prismatic Li-ion battery module operating at high ambient temperature. *Sci. China Technol. Sci.* **2020**, *63*, 2147–2153. [CrossRef]
39. Bai, F.; Chen, M.; Song, W.; Feng, Z.; Li, Y.; Ding, Y. Thermal management performances of PCM/water cooling-plate using for lithium-ion battery module based on non-uniform internal heat source. *Appl. Therm. Eng.* **2017**, *126*, 17–27. [CrossRef]
40. Wang, C.L.; Leong, J.C. Analysis of Thermal Management Strategies for 21,700 Lithium-Ion Batteries Incorporating Phase Change Materials and Porous Copper Foam with Different Battery Orientations. *Energies* **2024**, *17*, 1553. [CrossRef]

41. Leong, K.Y.; Saidur, R.; Kazi, S.N.; Mamun, A.H. Performance investigation of an automotive car radiator operated with nanofluid-based coolants (nanofluid as a coolant in a radiator). *Appl. Therm. Eng.* **2010**, *30*, 2685–2692. [CrossRef]
42. Drofenik, U.; Stupar, A.; Kolar, J.W. Analysis of Theoretical Limits of Forced-Air Cooling Using Advanced Composite Materials with High Thermal Conductivities. *IEEE Trans. Compon. Packag. Manuf. Technol.* **2011**, *1*, 528–535. [CrossRef]
43. Gammeter, C.; Krismer, F.; Kolar, J.W. Weight Optimization of a Cooling System Composed of Fan and Extruded-Fin Heat Sink. *IEEE Trans. Ind. Appl.* **2015**, *51*, 509–520. [CrossRef]
44. Lin, H.; Wang, Z.; Guo, X.; Lin, Z.; Chen, G. A 380 V/50 kVar SiC-SVG Achieving a Power Density of 1.652 kVar/L with the Optimization of Heatsink and Output Filter Volume. *IEEE J. Emerg. Sel. Top. Power* **2022**, *10*, 4634–4649. [CrossRef]
45. Lin, H.; Guo, X.; Chen, D.; Wu, S.; Chen, G. A Frequency Adaptive Repetitive Control for Active Power Filter With 380V/75A SiC-Inverter. *IEEE Trans. Ind. Appl.* **2022**, *58*, 5469–5479. [CrossRef]
46. Vasta, S. Adsorption Air-Conditioning for Automotive Applications: A Critical Review. *Energies* **2023**, *16*, 5382. [CrossRef]
47. Abdullah, M.O.; Tan, I.A.W.; Lim, L.S. Automobile adsorption air-conditioning system using oil palm biomass-based activated carbon: A review. *Renew. Sustain. Energy Rev.* **2011**, *15*, 2061–2072. [CrossRef]
48. Zhao, D.; Tan, G. A review of thermoelectric cooling: Materials, modeling and applications. *Appl. Therm. Eng.* **2014**, *66*, 15–24. [CrossRef]

Disclaimer/Publisher's Note: The statements, opinions and data contained in all publications are solely those of the individual author(s) and contributor(s) and not of MDPI and/or the editor(s). MDPI and/or the editor(s) disclaim responsibility for any injury to people or property resulting from any ideas, methods, instructions or products referred to in the content.